Free-boundary MRxMHD equilibrium calculations using the Stepped-Pressure Equilibrium Code

S. R. Hudson
Princeton Plasma Physics Laboratory, PO Box 451, Princeton NJ 08543, USA.

J. Loizu
École Polytechnique Fédérale de Lausanne, Swiss Plasma Center, CH-1015 Lausanne, Switzerland

C. Zhu
Princeton Plasma Physics Laboratory, PO Box 451, Princeton NJ 08543, USA

Z. S. Qu
Mathematical Sciences Institute, the Australian National University, Canberra ACT 2601, Australia

C. Nührenberg and S. Lazerson
Max-Planck-Institut für Plasmaphysik, 17491 Greifswald, Germany

C. B. Smiet
Princeton Plasma Physics Laboratory, P.O. Box 451, Princeton NJ 08543, USA.

M. J. Hole
Mathematical Sciences Institute, the Australian National University, Canberra ACT 2601, Australia and
Australian Nuclear Science and Technology Organisation,
Locked Bag 2001, Kirrawee DC NSW 2232, Australia
(Dated: February 19, 2020)

The stepped-pressure equilibrium code (SPEC) [Hudson *et al.*, Phys. Plasmas **19**, 112502 (2012)] is extended to enable free-boundary, multi-region relaxed magnetohydrodynamic (MRxMHD) equilibrium calculations. The vacuum field surrounding the plasma inside an arbitrary 'computational boundary', $\mathcal{D}$, is computed, and the virtual casing principle is used iteratively to compute the normal field on $\mathcal{D}$ so that the equilibrium is consistent with an externally produced magnetic field. Recent modifications to SPEC are described, such as the use of Chebyshev polynomials to describe the radial dependence of the magnetic vector potential, and a variety of free-boundary verification calculations are presented.

I. INTRODUCTION

Calculating the magnetohydrodynamic (MHD) equilibrium in magnetically confined plasma experiments, such as stellarators and tokamaks, is typically the starting point for most analyses of plasma confinement. Equilibrium calculations, and the associated linear and nonlinear stability analyses, are required for reconstruction of existing experiments and for the design of future experiments. Ignoring nonideal effects such as resistivity, viscosity, etc., the simplest equation describing static MHD equilibria is $\nabla p = \mathbf{j} \times \mathbf{B}$, called the ideal-force-balance equation, where p is the plasma pressure, $\mathbf{B}$ is the magnetic field, and $\mathbf{j} = \nabla \times \mathbf{B}/\mu_0$ is the current density. The magnetic field is produced by currents external and internal to the plasma, $\mathbf{B} = \mathbf{B}_C + \mathbf{B}_P$, where $\mathbf{B}_C$ is produced externally, by current-carrying coils for example, and $\mathbf{B}_P$ is produced by plasma currents.

The solutions to the ideal-force-balance equation can be complicated. For configurations without a continuous symmetry, so-called three-dimensional (3D) configurations, the magnetic field will typically not possess a smooth family of nested flux surfaces. 3D magnetic fields are analogous to $1\frac{1}{2}$-dimensional Hamiltonian systems [1], and such fields are generally non-integrable in a dynamical systems context [2, 3]. Even though the magnetic *field* may be quite smooth, the phase space, i.e., the properties of the magnetic field*lines*, is fractal, with invariant Kolmogorov-Arnold-Moser (KAM) surfaces [4, 5], cantori [6–9] and magnetic islands infinitely interspersed with the irregular trajectories of the ergodic "seas" [10] associated with the unstable manifolds of periodic field-lines.

The ideal-force-balance equation and $\nabla \cdot \mathbf{j} = 0$ lead to magnetic differential equations [11, 12] for the pressure, $\mathbf{B} \cdot \nabla p = 0$, and parallel current density, $\mathbf{B} \cdot \nabla \sigma = -\nabla \cdot \left(\mathbf{B} \times \nabla p / B^2\right)$, where we have written $\mathbf{j} = \sigma \mathbf{B} + \mathbf{B} \times \nabla p / B^2$. The consequence of having non-integrable magnetic fields and ensuring that $\mathbf{B} \cdot \nabla p = 0$, for example, are pressure profiles that were famously described by Grad as being "pathological" [13].

If the magnetic field is constrained to be integrable, i.e., constrained to possess a nested family of flux surfaces, which can be enforced by writing $\mathbf{B} = \nabla \times [\psi \nabla \theta - \chi(\psi) \nabla \zeta]$ where $2\pi\psi$ and $2\pi\chi$ are the toroidal and poloidal fluxes, then both integrable and non-integrable singular current densities may arise at a dense set of "resonances" where the the rotational transform, $\iota \equiv \partial\chi/\partial\psi$, is rational [14], and where the word "integrable" is used in a quadrature sense. An expanded discussion of the complexities of 3D MHD equilibrium calculations and existing theoretical and numerical approaches is given

earlier [15].

To eliminate the mathematical pathologies, building upon "sharp-boundary" models [16, 17], Bruno & Laurence [18] introduced the stepped-pressure equilibrium model, for which discontinuities in the pressure and magnetic field are allowed. Theorems reminiscent of the KAM theorem [4, 5] were presented guaranteeing the existence of well-defined solutions provided certain conditions are satisfied, namely that the discontinuities should coincide with surfaces with strongly irrational rotational transform. The stepped-pressure solutions do not impose topological constraints at the rational surfaces, and non-integrable (in a quadrature sense) singular current densities do not arise, and the pressure profile is not fractal. Even though the magnetic field and pressure are not everywhere differentiable, they are integrable (again, quadrature sense).

Dewar *et al.* introduced the multi-region relaxed magnetohydrodynamic (MRxMHD) energy principle [19–21], which is a unification of the ideal MHD energy principle introduced by Kruskal & Kulsrud [22] and Taylor relaxation [23, 24]. Extrema of the MRxMHD energy principle are stepped-pressure equilibria. The plasma is divided into a number of sub-regions that are separated by so-called "ideal" interfaces. The magnetic field is assumed to undergo Taylor relaxation in each region and satisfies the Beltrami equation $\nabla \times \mathbf{B} = \mu \mathbf{B}$ where μ is constant. In each region, the magnetic field is constrained to remain tangential to each interface, and the pressure is constant. Across the interfaces the thermal pressure may jump, but the sum of thermal and magnetic pressure is continuous.

Mills *et al.* [25] considered a generalisation to MRxMHD to allow alternate relaxed and ideal MHD regions and studied the stability. The high-n stability of the ideal interfaces was studied by Barmaz *et al.* [26]. Dennis *et al.* presented generalizations of MRxMHD that include flow [27] and pressure anisotropy [28], and Lingam *et al.* [29] presented a model of multi-region relaxed Hall MHD. The static model was extended to a dynamical model by Dewar *et al.* [30]. A generalization that accommodates everywhere continuous and differentiable magnetic fields and allows for magnetic islands and chaos has been described by Hudson & Kraus [31], and the resistive stability of this class of equilibria has been studied by Wright *et al.* [32].

The stepped-pressure equilibrium code (SPEC) [15] is based on the MRxMHD energy principle. SPEC was used by Dennis *et al.* [33] to investigate the formation of the single-helical and double-helical states in a reversed field pinch, and by Loizu *et al.* [34] to compute the pressure-driven $1/x$ and the δ-function singular current-densities in ideal-MHD equilibria with resonantly perturbed boundaries (this required taking the "ideal limit", in which MRxMHD reduces to ideal MHD [35]). A linearized version of SPEC and the full nonlinear version were verified against analytic calculations of resonant-magnetic-perturbation penetration in cylindrical geometry by Loizu *et al.* [36, 37]. Fixed-boundary vacuum calculations in strongly shaped stellarator geometries were verified [38] against a Biot-Savart code. SPEC was used to study the equilibrium β-limits in classical stellarators [39], the linear stability and nonlinear saturation of the tearing mode [40, 41], and flow relaxation in reversed-field-pinch sawtooth events [42].

This paper describes the extension of SPEC from a fixed-boundary code to a free-boundary code. Many aspects of free-boundary SPEC are identical to fixed-boundary SPEC, and we will assume that the reader is familiar with our earlier paper [15]. To clarify terminology: fixed-boundary equilibrium codes determine the equilibrium magnetic field consistent with the given plasma boundary and the given plasma profiles. Free-boundary calculations are required to determine the position of the plasma boundary, and the equilibrium magnetic field, given the externally applied magnetic field and the plasma profiles. Free-boundary 3D MHD calculations in stellarator geometry have been performed using the VMEC [43], PIES [44], NIMROD [45], HINT-2 [46], SIESTA [47] and BIEST [48] codes, and the M3D-C^1 code [49] is being extended to accommodate stellarator geometries. (The GVEC code, which similar to VMEC but accommodates discontinuities, is presently under construction [50].)

The outline of this paper is as follows. First, for completeness, a brief description of MRxMHD and SPEC is presented. The numerical discretization employed by SPEC and various recent code modifications are described. These include: using Chebyshev polynomials to represent the radial dependence of the Fourier harmonics of the vector potential; the inclusion of the non-"stellarator-symmetric" terms in the representation of the geometry and the magnetic vector potential, so that equilibria with arbitrary geometries can be computed; the augmentation of the fixed-boundary calculation with a vacuum field, which is calculated in a additional region outside the plasma boundary and inside an arbitrary "computational boundary"; the implementation of a virtual-casing method for calculating the magnetic field produced by the plasma currents at a location external to the plasma; and a description of a Picard scheme to determine the self-consistent value of the differential flux on the computational boundary. Some example verification calculations are then presented.

II. FREE-BOUNDARY MRXMHD

The classic MHD energy functional [22] is given by

$$W \equiv \int_{\mathcal{V}} \left(\frac{p}{\gamma - 1} + \frac{B^2}{2} \right) dv, \tag{1}$$

where $\mathcal{V}$ is the plasma volume enclosed by the plasma boundary, $\partial\mathcal{V}$, to which the magnetic field is tangential. The pressure, p, and current density, $\mathbf{j}$, are re-scaled by the constant μ_0 and should be interpreted as $\mu_0 p$ and $\mu_0 \mathbf{j}$, and similarly for W. Restricting attention to so-called ideal variations in the pressure, extremizing solutions satisfy the ideal force-balance condition, $\nabla p = \mathbf{j} \times \mathbf{B}$ [22].

Ideal variations constrain the topology of structures traced out by the magnetic fieldlines. MRxMHD allows

for a less-restrictive class of variations and for the magnetic field to "tear", and so magnetic islands and chaotic fieldlines can emerge. Some constraints are included to avoid globally relaxed solutions.

The "relaxed" aspect of MRxMHD follows Taylor relaxation [23], namely that weakly resistive plasmas will dynamically evolve to minimize the energy but the magnetic helicity,

$$K \equiv \int_{\mathcal{V}} \mathbf{A}\cdot\mathbf{B}\, dv, \tag{2}$$

is conserved [24, 51], where $\mathbf{A}$ is a magnetic potential, $\mathbf{B} = \nabla\times\mathbf{A}$. The magnetic helicity is not gauge invariant if the volume of integration is not simply connected [52]; however, the choice of gauge does not alter the physics. (The gauge constraints used in SPEC are described earlier [15].) Taylor states are constructed mathematically by finding the minimum of W subject to the constraint $K = K_o$, i.e., by finding extrema of $\mathcal{F} \equiv W - \mu(K - K_o)/2$ where μ is the "helicity multiplier", and the factor of $^{-1}/_{2}$ is introduced for convenience. Allowing for variations in $\mathbf{A}$ that preserve the toroidal flux and the boundary condition $\mathbf{B}\cdot\mathbf{n} = 0$ where $\mathbf{n}$ is normal but are otherwise arbitrary, and with the only constraint on the pressure being $pV^\gamma = P$, where V is the volume of $\mathcal{V}$ and P is an "adiabatic" constant, magnetic fields that extremize $\mathcal{F}$ satisfy $\nabla\times\mathbf{B} = \mu\mathbf{B}$ and $p = P/V^\gamma$.

The "multi-region" component of MRxMHD is to partition the plasma into a finite number, N_V, of subregions, $\mathcal{V}_v$, separated by nested interfaces, $\mathcal{I}_v$, for $v = 1,\ldots,N_V$ with $\mathcal{I}_{N_V} = \partial\mathcal{V}$. The magnetic field is constrained to satisfy $\mathbf{B}\cdot\mathbf{n} = 0$ on each side of each interface, and the fluxes in each region are constrained.

For *fixed*-boundary calculations, only the *internal* interfaces, $\mathcal{I}_v$ for $v = 1,\ldots,N_V - 1$, are allowed to change. These can move but "ideal constraints" are enforced, by which we mean that the geometry of the interfaces and the magnetic field move together so the interfaces remain flux surfaces and the enclosed fluxes are conserved. The interfaces constitute barriers that frustrate global relaxation.

The MRxMHD energy principle is to minimize the plasma energy subject to the constraints of conserved helicity in *each* of the $\mathcal{V}_v$. The energy functional is

$$\mathcal{F} = \sum_{v=1}^{N_V} \left[W_v - \mu_v\left(K_v - K_{o,v}\right)/2\right], \tag{3}$$

where W_v and K_v are the energy and helicity integrals as given in Eqn. 1 and Eqn. 2 but restricted to the v-th volume. The magnetic field in each $\mathcal{V}_v$ is constrained to remain tangential to the $\mathcal{I}_v$, but within each volume the topology of the field is unconstrained. (In the limit $N_v \to \infty$ of infinitely many ideal interfaces, the topology is constrained everywhere [35].)

The Euler-Lagrange equations [15] for extremizing states are: in each $\mathcal{V}_v$ the magnetic field is a linear force-free field, $\nabla\times\mathbf{B}_v = \mu_v\mathbf{B}_v$; and across each of the $\mathcal{I}_v$ the total pressure is continuous, $[[p + B^2/2]] = 0$. To avoid a problem of small-divisors, the rotational transforms on the interfaces are generally required to be strongly irrational [18, 53]. Extremizing solutions are the stepped-pressure states of Bruno & Laurence.

In each $\mathcal{V}_v$, given the geometry of the adjacent interfaces, there are three parameters that define the solution for the magnetic field: the enclosed toroidal and poloidal fluxes, $\Delta\psi_{t,v}$ and $\Delta\psi_{p,v}$, and the helicity, $K_{o,v}$. The toroidal and poloidal fluxes are given by poloidal and toroidal loop integrals of the vector potential. (In the innermost toroidal volume, only the enclosed toroidal flux and helicity are defined.)

As typical for Lagrange multipliers, the helicity multipliers, μ_v, must be adjusted to enforce the helicity constraints. Alternatively, it is sometimes desirable to constrain μ_v, which is related to the parallel current-density, $\mu_v = \mathbf{j}_v\cdot\mathbf{B}_v/B_v^2$. In this case the helicity will only be known *a posteriori*. It is also sometimes desirable to allow the value of $K_{o,v}$ and μ_v, and either one or both of $\Delta\psi_{t,v}$ and $\Delta\psi_{p,v}$ to vary in order to obtain solutions with, for example, prescribed rotational transform on the interfaces, or to constrain the currents passing through certain surfaces.

A. Extension to free-boundary

To extend the fixed-boundary calculation to a free-boundary, an additional region that lies outside the plasma boundary is included, in which the vacuum magnetic field is calculated. Vacuum fields satisfy $\nabla\times\mathbf{B} = 0$ and so are of course a special class of Beltrami fields; we just set $\mu = 0$. The existing numerical architecture can be employed to calculate the vacuum field.

Before proceeding, we momentarily digress to explain a numerical detail that might interest some readers. SPEC writes the magnetic field as the curl of the magnetic vector potential, $\mathbf{B} = \nabla\times\mathbf{A}$. It is of course possible in the vacuum region to employ the scalar potential, i.e. to write $\mathbf{B} = \nabla\Phi$, where $\Phi = I\,\theta + G\,\phi + \tilde{\Phi}(s,\theta,\phi)$, where I and G are the net toroidal plasma and linking currents, and where $\tilde{\Phi}(s,\theta,\phi)$ is a single-valued function of position. This offers the advantage that both the vacuum condition, $\nabla\times\mathbf{B} = 0$, and I and G can be satisfied/specified exactly regardless of numerical resolution. There is the additional advantage that the scalar potential is described using a single function of position, namely $\tilde{\Phi}$, whereas the magnetic vector potential is described by two, namely A_θ and A_ϕ (assuming that gauge freedom is used to remove the third component of the vector potential, A_s). However, both the condition that $\nabla\cdot\mathbf{B} = 0$ and the boundary condition $\mathbf{B}\cdot\mathbf{n} = 0$ at the interfaces become subject to "numerical-resolution" error. For these reasons, we use the magnetic vector potential to describe the vacuum field.

The inner boundary of the additional vacuum region coincides with the plasma boundary, on which the constraint $\mathbf{B}\cdot\mathbf{n} = 0$ is enforced. The outer boundary, $\mathcal{D}$, hereafter called the "computational boundary", is arbitrary except that, for expediency, it must lie between the plasma boundary and the external current-carrying coils.

The normal magnetic field on $\mathcal{D}$ is generally *not* zero,

and the enclosed toroidal and poloidal fluxes, $\Delta\psi_t$ and $\Delta\psi_p$, in the vacuum region are not well-defined physical quantities. The relevant physical quantities are instead the total toroidal plasma current, I, and the total current linking the toroidal plasma volume, G. As will be described in the following, $\Delta\psi_t$ and $\Delta\psi_p$ in the vacuum region can be iteratively adjusted to enforce constraints on I and G.

Given the geometry of $\mathcal{D}$, e.g. $\mathbf{x}(\theta,\phi)$, where θ is an arbitrary poloidal angle and ϕ is the geometric cylindrical angle, the magnetic flux through an infinitesimal area element of $\mathcal{D}$ is $D\,d\theta\,d\phi \equiv \mathbf{B}\cdot\mathbf{x}_\theta\times\mathbf{x}_\phi\,d\theta\,d\phi$, where $\mathbf{x}_\theta \equiv \partial\mathbf{x}/\partial\theta$ and $\mathbf{x}_\phi \equiv \partial\mathbf{x}/\partial\phi$. The differential flux has two components, $D^n = D_C + D_P^n$. The first part, D_C, is that produced externally (by either a given or assumed set of current carrying coils, for example, or permanent magnets [54]). This article shall primarily consider the case that the free-boundary equilibrium for a *given* external field is required, and D_C is required as input. The second part, D_P^n, is produced by the plasma currents and is *a priori* unknown. (Except for the special case of vacuum fields when we know that $D_P^n = 0$.) If D_C is given, then the self-consistent value of D_P^n must be computed iteratively. The superscript n is used to label iterations.

The value of D^n on $\mathcal{D}$ must be provided as a boundary condition in order to solve for the magnetic field in the vacuum region. To initialize the free-boundary calculation a reasonable initial guess is required. Choosing $D_P^0 = -D_C$, for example, will initially force a flux surface in the vacuum region to coincide with $\mathcal{D}$. Other constructions of the initial guess for D_P are described in Sec. IV.

The geometry of the interfaces, $\mathcal{I}_v$ for $v = 1,\ldots,N_V$, which for free-boundary calculation includes the plasma boundary, are adjusted iteratively to achieve force balance, $[[p + B^2/2]] = 0$, across each of the $\mathcal{I}_v$. The geometry of the computational boundary, $\mathcal{D}$, and the external differential flux, D_C, need not change during the calculation.

After force-balance is achieved for the provided D^n, the virtual casing principle is used to compute the D_P^{n+1} that is consistent with the computed equilibrium. This, generally, will differ from $D_P^n = D^n - D_C$, and the vacuum field must be recomputed, and to re-establish force balance across the plasma boundary the geometry of the interfaces must be recomputed.

III. NUMERICAL IMPLEMENTATION

Following the convention used in the VMEC code, all even doubly periodic functions, e.g. $R(\theta,\phi)$, are written

$$\begin{aligned} R(\theta,\phi) &\equiv \sum_i R_i\cos(\alpha_i) \\ &\equiv \sum_{n=0}^{N} R_{0,n}\cos(-nN_P\phi) \\ &+ \sum_{m=1}^{M}\sum_{n=-N}^{N} R_{m,n}\cos(m\theta - nN_P\phi), \end{aligned} \quad (4)$$

where for brevity we write $\alpha_i \equiv m_i\theta - n_i\phi$, the Fourier resolutions are M and N, and N_P is the field periodicity, which below is frequently omitted for brevity. Similarly for odd functions. The notation "f_i" is used to indicate the (m_i, n_i) Fourier harmonic of the function $f(\theta,\phi)$.

The equilibrium calculation is initialized by providing a reasonable initial guess for the geometry of the interfaces,

$$\mathbf{x}_v(\theta,\phi) \equiv R_v(\theta,\phi)\,\hat{r} + Z_v(\theta,\phi)\,\hat{k}, \quad (5)$$

where $\hat{r} \equiv \cos\phi\,\hat{i} + \sin\phi\,\hat{j}$ is the unit radial vector, and $R_v \equiv \sum_i \left(R^c_{v,i}\cos\alpha_i + R^s_{v,i}\sin\alpha_i\right)$, and similarly for Z_v, where the superscripts "c" and "s" merely indicate the cosine and sine harmonics. The v-th volume is bounded by $\mathbf{x}_{v-1}$ and $\mathbf{x}_v$. SPEC can operate in Cartesian "slab" [34], cylindrical [36, 37] and toroidal [15] geometry; but, for brevity, the following will restrict attention to the toroidal case. SPEC also allows for non-stellarator-symmetric geometry [55]; but, again for brevity, the following shall display only the stellarator-symmetric terms. Stellarator symmetry [55] means that the $R_v(\theta,\phi)$ can be written as a cosine series and $Z_v(\theta,\phi)$ as sine, and the "c" and "s" superscripts shall be omitted when this causes no confusion.

Given the $\mathcal{I}_v$ for $v = 1,\ldots,N_V$ and $\mathcal{I}_{N_V+1} \equiv \mathcal{D}$, a continuous toroidal coordinate framework is constructed by interpolation. In the *annular* volumes, $\mathcal{V}_v$ for $v = 2,\ldots,N_V+1$, which are bounded by $\mathcal{I}_{v-1}$ and $\mathcal{I}_v$, the toroidal coordinates are defined by $\mathbf{x}(s,\theta,\phi) \equiv \frac{1}{2}(1-s)\,\mathbf{x}_{v-1}(\theta,\phi) + \frac{1}{2}(1+s)\,\mathbf{x}_v(\theta,\phi)$, where the "local" radial coordinate, s, varies from $s=-1$ to $s=+1$. A global radial coordinate is not required because the magnetic field in each region is computed in parallel.

In the innermost *simple-torus* volume, $\mathcal{V}_1$, which is bounded by $\mathcal{I}_1 \equiv \mathbf{x}_1(\theta,\phi)$, the coordinates are constructed by first choosing the "geometric center" of $\mathcal{I}_1$,

$$R_0(\phi) \equiv \oint R_1(\theta,\phi)\,dl \Big/ \oint dl\,, \quad (6)$$

$$Z_0(\phi) \equiv \oint Z_1(\theta,\phi)\,dl \Big/ \oint dl\,, \quad (7)$$

to be the coordinate axis, where $dl/d\theta \equiv \sqrt{\partial_\theta R_1(\theta,\phi)^2 + \partial_\theta Z_1(\theta,\phi)^2}$. The coordinate axis so defined depends only on the geometry of the innermost interface (and thus the block tri-diagonal structure of the force-gradient matrix is preserved). There is no assumed relationship between the coordinate axis and the magnetic axis. Introducing $\bar{s} \equiv (s+1)/2$ so that $\bar{s} \in [0,1]$, the coordinates in the innermost volume are defined by the following "regularized" interpolation,

$$R_{1,i}(s) = R_{0,i} + (R_{1,i} - R_{0,i})f_i, \quad (8)$$

where $f_i = \bar{s}$ for $m_i = 0$, and $f_i = \bar{s}^{m_i/2}$ for $m \neq 0$; and similarly for the $Z_{1,i}(s)$. Such a construction encourages, but does not guarantee, that the coordinate surfaces will not intersect. The effective minor radius scales like $r \sim \sqrt{s}$.

A Fourier-Chebyshev representation is used for the vector potential, $\mathbf{A}_v$, in each volume. An appropriate gauge [15] allows $\mathbf{A} = A_\theta\nabla\theta + A_\phi\nabla\phi$, where the volume

index v has been suppressed for clarity. The components of the vector potential are written

$$A_\theta(s,\theta,\phi) \;=\; \sum_i \sum_{l=0}^{L} A_{\theta,i,l}\; T_l(s)\cos\alpha_i, \qquad (9)$$

where L describes the Chebyshev resolution in a given region, and similarly for $A_\phi(s,\theta,\phi)$. Additional odd (i.e., sine) harmonics are included for the non-stellarator-symmetric case. The Chebyshev polynomials, $T_l(s)$, are determined using recurrence relations: $T_0(s)=1$, $T_1(s)=s$, and $T_l(s)=2\,s\,T_{l-1}(s)-T_{l-2}(s)$. To accommodate the coordinate singularity that arises at the coordinate axis, in the innermost toroidal region this representation is augmented with "radial regularization factors", so that $T_l(s)\cos\alpha_i$ becomes $\bar{s}^{m_i/2}T_l(s)\cos\alpha_i$. (This regularization causes an ill-conditioning problem, which is discussed later in this article.)

Coordinate surfaces coincide with the $\mathcal{I}_v$ and $\mathcal{D}$, and by design this makes it easy to enforce the constraints that $\mathbf{B}\cdot\mathbf{x}_\theta\times\mathbf{x}_\phi=0$ on the $\mathcal{I}_v$ and $\mathbf{B}\cdot\mathbf{x}_\theta\times\mathbf{x}_\phi=D^n$ on $\mathcal{D}$. Elsewhere in the relaxed volumes there is no relationship between the coordinates and the magnetic field, which at this stage of the calculation is yet to be determined.

The boundary condition that $\mathbf{B}\cdot\mathbf{x}_\theta\times\mathbf{x}_\phi=0$ at the inner boundary of each region and the remaining gauge freedom is constrained by requiring that $A_\theta(-1,\theta,\phi)=0$ and $A_\phi(-1,\theta,\phi)=0$. (An expanded description of the boundary conditions and gauge constraints is described earlier [15].) The condition that $\mathbf{B}\cdot\mathbf{x}_\theta\times\mathbf{x}_\phi=D^n$ at the outer boundary requires that $\partial_\theta A_\phi(+1,\theta,\phi)-\partial_\phi A_\theta(+1,\theta,\phi)=D^n$. This condition, and the constraints on the enclosed toroidal and poloidal fluxes, $\Delta\psi_{t,v}$ and $\Delta\psi_{p,v}$, and the helicities, $K_{o,v}$, in each region are enforced using Lagrange multipliers.

To compute the Beltrami fields in each volume we can ignore the pressure, which only impacts the constraint of force balance, $[[p+B^2/2]]=0$, *across* the interfaces. Assuming the geometry of the interfaces and $\boldsymbol{\psi}\equiv\{\Delta\psi_{t,v},\Delta\psi_{p,v},K_{o,v},D_i^n\}$ are given, where D_i^n are the Fourier harmonics (odd, in the case of stellarator symmetry) of the differential flux on the outer boundary, the degrees-of-freedom in the constrained energy functional in each volume are the coefficients of the Fourier-Chebyshev representation for the vector potential and the Lagrange multipliers. (To obtain a uniform treatment for all volumes, we have allowed for a non-zero D_i^n on the outer boundary of each volume; in practice, however, it is only on $\mathcal{D}$ that the D_i^n can be non-zero.)

Writing $\mathbf{a}\equiv\{A_{\theta,i,l},A_{\phi,i,l},a_i,b_i,c_1,d_1,e_i\}$ to represent the degrees-of-freedom in the vector potential and the Lagrange multipliers — *except* for the helicity multiplier, μ, which is treated separately — and dropping the "v" subscript for notational clarity, the constrained energy functional in each volume is

$$\begin{aligned}
&\mathcal{F}(\mathbf{a},\mu,\boldsymbol{\psi})\\
&= \frac{1}{2}\int_{\mathcal{V}}\mathbf{B}\cdot\mathbf{B}\;dv\\
&- \frac{\mu}{2}\left[\int_{\mathcal{V}}\mathbf{A}\cdot\mathbf{B}\;dv - K_o\right]\\
&+ a_i\left[\sum_l A_{\theta,i,l}T_l(-1)\right]\\
&+ b_i\left[\sum_l A_{\phi,i,l}T_l(-1)\right]\\
&+ c_1\left[\sum_l A_{\theta,1,l}T_l(+1) - \Delta\psi_t\right]\\
&+ d_1\left[\sum_l A_{\phi,1,l}T_l(+1) - \Delta\psi_p\right]\\
&+ e_i\left[\sum_l \left(-m_iA_{\phi,i,l} - n_iA_{\theta,i,l}\right)T_l(+1) - D_i^n\right], \qquad (10)
\end{aligned}$$

where the a_i and b_i are Lagrange multipliers used to enforce the combined gauge and boundary conditions on the inner boundary, c_1 and d_1 are Lagrange multipliers used to enforce the enclosed flux constraints, and the e_i are Lagrange multipliers used to enforce the boundary condition for each Fourier harmonic of $\mathbf{B}\cdot\mathbf{x}_\theta\times\mathbf{x}_\phi=D^n$ on the outer boundary; and summation over i is assumed. (Note: a_i should not be confused with the i-th element of the vector $\mathbf{a}$.)

The energy functional is written as

$$\mathcal{F} = \tfrac{1}{2}\mathbf{a}^T\cdot\mathcal{A}\cdot\mathbf{a} - \tfrac{1}{2}\mu\left(\mathbf{a}^T\cdot\mathcal{B}\cdot\mathbf{a}-K_o\right) + \mathbf{a}^T\cdot\mathcal{C}\cdot\mathbf{b}, \qquad (11)$$

where $\mathcal{A}$, $\mathcal{B}$ and $\mathcal{C}$ are matrices and $\mathbf{b}$ contains the boundary conditions, namely $\{\Delta\psi_t,\Delta\psi_p,D_i^n\}$. The matrices $\mathcal{A}$, $\mathcal{B}$ and $\mathcal{C}$ are constructed by inserting the representation for the vector potential given in Eqn. 9 into Eqn. 10 and computing the appropriate volume integrals of the products of the Chebyshev polynomials, their derivatives, and various trigonometric terms. The matrix $\mathcal{A}$ depends on the coordinate metrics and Jacobian, and thus on the geometry of the adjacent interfaces, and so needs to be re-calculated if the interface geometry changes. The matrices $\mathcal{B}$ and $\mathcal{C}$ do not depend on the interface geometry.

The required volume integrals are computed using a mixed "Fourier-Gaussian" quadrature method:

$$\begin{aligned}
&\int_{-1}^{+1}\int_0^{2\pi}\int_0^{2\pi} f(s,\theta,\phi)\;d\phi\,d\theta\,ds\\
&\approx\; 4\pi^2\sum_{p=0}^{P}\omega_p\,f_1(s_p), \qquad (12)
\end{aligned}$$

where a fast Fourier transform (FFT) provides $f=\sum_i f_i\cos\alpha_i$, and the ω_p and s_p are the weights and abscissae for a Gaussian integration of resolution P. The required resolution of the Gaussian integration, P, is related to the Chebyshev resolution, L.

The extremizing magnetic fields consistent the provided constraints are determined by solving $\nabla_{\mathbf{a},\mu}\mathcal{F}=0$.

If the parallel current in each region, $\mu = \mathbf{j}\cdot\mathbf{B}/B^2$, rather than the helicity were constrained, then μ may be treated as a prescribed parameter rather than as an independent degree of freedom (and it is to accommodate this desideratum that μ is treated separately). In the vacuum region, for example, we must set $\mu = 0$. $\mathcal{F}$ then becomes quadratic in $\mathbf{a}$ and $\nabla_{\mathbf{a}}\mathcal{F} = 0$ reduces to a set of linear equations,

$$(\mathcal{A} - \mu\,\mathcal{B})\cdot\mathbf{a} = -\,\mathcal{C}\cdot\mathbf{b}. \tag{13}$$

Generally, however, to be consistent with the method of Lagrange multipliers, μ must be treated as an independent degree-of-freedom that is to be adjusted in order to enforce the helicity constraint. Nonlinear iterative methods, like the Newton method or the Sequential Quadratic Programing (SQP) method, can be used to find extrema of Eqn. 11. Once the $\mathcal{A}$, $\mathcal{B}$ and $\mathcal{C}$ are computed, only matrix-vector products are required.

After the magnetic fields in each region are determined, it is possible to calculate the rotational transform on the interfaces and the enclosed plasma currents. Depending on the solution that one seeks (that is, depending on whether the helicity profile, the current profile, or the rotational-transform profile is prescribed), these may be used to constrain the calculation.

A straight fieldline angle, θ_s, may be constructed on flux surfaces by writing $\theta_s \equiv \theta + \lambda$, where $\lambda = \sum_i \lambda_i \sin\alpha_i$, (only sine terms are required for stellarator symmetry), and by insisting that

$$\frac{\mathbf{B}\cdot\nabla\theta_s}{\mathbf{B}\cdot\nabla\phi} = \dot\theta(1+\lambda_\theta) + \lambda_\phi = \imath, \tag{14}$$

where $\dot\theta \equiv B^\theta/B^\phi$ and $\boldsymbol{\lambda} \equiv (\imath, \lambda_2, \lambda_3, \dots)^T$ is to be determined, and $\lambda_\theta \equiv \partial_\theta\lambda$ and $\lambda_\phi \equiv \partial_\phi\lambda$. This becomes

$$\partial_s A_\theta\,\imath + \partial_s A_\phi\,\lambda_\theta - \partial_s A_\theta\,\lambda_\phi = -\partial_s A_\phi. \tag{15}$$

Given the vector potential, equating Fourier coefficients gives a set of linear equations for $\boldsymbol{\lambda}$, which includes $\imath$.

There is a quirk associated with rational-rotational-transform surfaces: the transformation to the straight fieldline angle is not unique (the resonant harmonics are not constrained); nevertheless, the rotational transform is still well-defined. On the rational surfaces, the set of linear equations defined by Eqn. 15 can be solved using singular-value decomposition.

Given that sheet currents on the "ideal" interfaces are both mathematically admissible and physically meaningful in the context of ideal MHD [36], the transformation to the straight fieldline angle may take different values on either side of the interface. The rotational transform on the "inner" side of $\mathcal{I}_v$ is determined by the tangential field in $\mathcal{V}_v$, and that on the "outer" side by the tangential field in $\mathcal{V}_{v+1}$. For an *a priori* specification of $\{\Delta\psi_{t,v}, \Delta\psi_{p,v}, K_{o,v}\}$ in each subregion, or $\{\Delta\psi_{t,v}, \Delta\psi_{p,v}, \mu_v\}$ if the helicity-multiplier is to be constrained, the rotational transform on the interfaces can only be determined *a posteriori*. The calculation of the Beltrami field in each region is independent of the calculation in any other region (except that the boundaries of adjacent regions must coincide), and generally the rotational transform is not continuous across the interfaces.

To constrain the rotational transform on each side of each $\mathcal{I}_v$, and keeping the constraint of conserved enclosed toroidal flux in each region, it is generally required to iterate on $\Delta\psi_{p,v}$ and either $K_{o,v}$ or μ_v. A similar argument holds for the enclosed currents.

The total current passing through a given surface is determined by a surface integral of the current-density,

$$\int_{\mathcal{S}} \mathbf{j}\cdot d\mathbf{s} = \oint_{\partial\mathcal{S}} \mathbf{B}\cdot d\mathbf{l}\,. \tag{16}$$

The total toroidal plasma current, including any sheet currents that may lie on the plasma boundary, is obtained by taking a "poloidal loop", $d\mathbf{l} \equiv \mathbf{e}_\theta\,d\theta$, lying on the inner surface of the vacuum region (i.e., on the immediate outside of the plasma boundary), to obtain

$$I = \int_0^{2\pi} (-\partial_s A_\phi\; g_{\theta\theta} + \partial_s A_\theta\; g_{\theta\phi})\,/\sqrt{g}\,d\theta. \tag{17}$$

The linking current through the torus is obtained by taking a "toroidal loop", $d\mathbf{l} \equiv \mathbf{e}_\phi\,d\phi$, on the plasma boundary to obtain

$$G = \int_0^{2\pi} (-\partial_s A_\phi\; g_{\theta\phi} + \partial_s A_\theta\; g_{\phi\phi})\,/\sqrt{g}\,d\phi. \tag{18}$$

To obtain prescribed values for I and G, the values of $\Delta\psi_{t,v}$ and $\Delta\psi_{p,v}$ in the vacuum region must be adjusted.

Having computed the Beltrami fields in each volume consistent with the desired constraints (on either the helicities, parallel currents or the rotational transforms) and with the appropriate toroidal plasma and coil linking currents, it is then required to iteratively adjust the geometry of the $\mathcal{I}_v$ to satisfy force balance, $[[p + B^2/2]] = 0$, across the interfaces. For this, a variety of methods can be used. The present "default" method in SPEC is to use a multi-dimensional Newton method to iteratively determine the geometry of the $\mathcal{I}_v$. Matrix-perturbation calculations can be used to determine how the Beltrami field in each sub-region changes as the geometry of the adjacent interfaces change, and this can be used to compute the "force-gradient", namely the derivative of $[[B^2]]$ with respect to the interface geometry. (A suitable eigenvalue analysis of the force-gradient matrix can infer linear stability of the computed equilibrium.) Additional "spectral constraints" are included to constrain the tangential degrees-of-freedom in the poloidal parameterization [15, 56, 57].

There is an additional step that is required to obtain free-boundary equilibria consistent with supplied external magnetic fields: to determine the self-consistent differential flux at $\mathcal{D}$ produced by the plasma currents. For this, the virtual-casing principle [58–60] is used.

Given the tangential field on the plasma boundary,

$$\mathbf{B}_s = B^\theta\mathbf{e}_\theta + B^\phi\mathbf{e}_\phi, \tag{19}$$

the virtual-casing principle shows that the magnetic field at a point, $\bar{\mathbf{x}}$, outside the plasma – for this application in particular, namely a point on $\mathcal{D}$ – that is produced by

internal plasma currents is equivalent to the field generated by the surface current, $\mathbf{j} = \mathbf{n} \times \mathbf{B}_s$, on the plasma boundary, where $\mathbf{n}$ is the outward unit normal. The field created by this surface current is given by

$$\mathbf{B}(\bar{\mathbf{x}}) = -\frac{1}{4\pi} \int_{\mathcal{S}} \frac{(\mathbf{B}_s \times d\mathbf{s}) \times \hat{\mathbf{r}}}{r^2}, \tag{20}$$

where $\mathcal{S}$ is the plasma boundary, and $d\mathbf{s} \equiv \mathbf{e}_\theta \times \mathbf{e}_\phi \, d\theta \, d\phi$.

After the geometry of the interfaces have been adjusted to satisfy force balance for a given $D^n = D^n_P + D_C$, the differential flux at $\mathcal{D}$ produced by the plasma currents consistent with the *constructed* state, $D_{P,vc}$, can be determined by taking the dot product of the field produced by Eqn. 20 and $\mathbf{e}_\theta \times \mathbf{e}_\phi$ on $\mathcal{D}$.

Generally, $D_{P,vc}$ will not be the same as $D^n_P = D^n - D_C$ supplied as a boundary condition to compute the vacuum field to begin with. We note parenthetically that the equilibrium calculation can terminate at this point if the externally provided field can be recomputed to provide $D_C = D^n - D_{P,vc}$. If D_C is not allowed to change, a practical method for determining the self-consistent D^n_P is enabled using Picard iterations defined as follows: the normal field used for the next "free-boundary iteration" is given by

$$D^{n+1}_P = \lambda \, D^n_P + (1 - \lambda) D_{P,vc}, \tag{21}$$

where λ is a blending parameter included for numerical stability (which is *not* related to the transformation to the straight fieldline angle). These iterations are converged when $|D_{P,vc} - D^n_P|$ is less than a user-provided tolerance.

To summarize the required input information: A specific *fixed*-boundary SPEC equilibrium is described by the plasma boundary $\partial\mathcal{V}$, the number of subregions N_V, the pressure, the enclosed toroidal and poloidal fluxes, and the helicity in each subregion, $\{p_v, \Delta\psi_{t,v}, \Delta\psi_{p,v}, K_{o,v}\}$. Alternatively, the helicity multiplier itself may be given directly, so that the equilibrium is described by $\{p_v, \Delta\psi_{t,v}, \Delta\psi_{p,v}, \mu_v\}$. It is also possible to define the equilibrium by providing the rotational transform on the inner and outer side of each interface, so that the equilibrium is defined by $\{p_v, \Delta\psi_{t,v}, \iota^-_v, \iota^+_v\}$. This will generally require an iteration over both $\Delta\psi_{p,v}$ and μ_v for a given $\Delta\psi_{t,v}$. The total toroidal flux is $\Psi \equiv \sum_{v=1}^{N_V} \Delta\psi_{t,v}$. To define and compute a specific *free*-boundary equilibrium, it is required to also provide: (i) a computational boundary, $\mathcal{D}$, that lies outside the expected location of the plasma boundary (and inside the external coils, if external coils are assumed to provide the external field, $\mathbf{B}_C$), (ii) the Fourier harmonics of the differential flux at $\mathcal{D}$, $D_{C,i} \equiv (\mathbf{B}_C \cdot \mathbf{x}_\theta \times \mathbf{x}_\phi)_i$, that is produced externally; and (iii) the total toroidal plasma and coil linking currents, I and G.

IV. VERIFICATION CALCULATIONS

Non-axisymmetric configurations offer the significant advantage of having rotational transform with no plasma currents [61, 62] and constitute excellent opportunities for verification calculations.

We present 3 "vacuum" verification calculations. The first shows that $|\nabla \times \mathbf{B}| \to 0$ as the numerical resolution is increased, the second that SPEC reproduces an analytic solution, and the third that SPEC reproduces the field as computed using the Biot-Savart law given an external current distribution. Each of these calculations tests different aspects of the algorithm.

For vacuum fields, we must set the pressure, the helicity multipliers, the total toroidal plasma current all to be zero, i.e., $p_v = 0$, $\mu_v = 0$ and $I = 0$. The Beltrami fields in each region are parameterized by $\Delta\psi_{t,v}$ and $\Delta\psi_{p,v}$. The differential magnetic flux at $\mathcal{D}$ produced by the plasma currents is (of course) zero for vacuum fields, i.e., $D_P = 0$, and consequently the virtual casing calculation of $D_{P,vc}$ and the Picard scheme for calculating the self-consistent value of D_P are not required.

Following the vacuum verification calculations, various calculations are performed that test the veracity of the virtual casing calculation and the Picard scheme for computing the self-consistent value of D_P for equilibria with non-zero plasma currents.

For all free-boundary SPEC calculations, the only information required from the external magnetic field is (i) the differential flux that is produced externally, D_C, on a suitable computational boundary, $\mathcal{D}$, and (ii) the total linking current, $G = \mu_0 I_C$, where I_C is the total amount of current passing through the torus hole.

A. "Self"-verification in vacuum.

The simplest vacuum calculation is to choose there to be only one plasma volume, $N_V = 1$. We consider a set of coils that produces a stellarator symmetric, vacuum magnetic field with a rotating elliptical structure with 5 field periods, as shown in Fig. 1. The computational boundary, $\mathcal{D}$, is chosen to be a torus with circular cross-section, $R = R_0 + a\cos\theta$ and $Z = -a\sin\theta$, with $R_0 = 10$ and $a = 1.58$. Using the Biot-Savart law, we compute the differential magnetic flux, D_C, produced by the coils on the computational boundary, $\mathcal{D}$.

In this $N_V = 1$ calculation, the value of the toroidal flux in the plasma region, $\Delta\psi_{t,1}$, which is also the total toroidal flux, Ψ, is somewhat arbitrary. Choosing a larger value of Ψ only enlarges the plasma region and does not change the solution for the magnetic field; however, the value of Ψ should not be chosen so large that the plasma boundary lies outside $\mathcal{D}$ or in a region of islands and chaos. In the latter case, a solution without sheet currents *cannot* be found. (The existence of a flux surface with enclosed toroidal flux Ψ for a prescribed magnetic field is related to the KAM theorem.) Here we choose $\Psi = 0.17\Psi_0$, where Ψ_0 is the toroidal flux passing through the surface defined by $\mathcal{D}$ at the toroidal angle $\phi = 0$.

SPEC finds an equilibrium by adjusting the geometry of the single interface $\equiv$ plasma boundary until force imbalance is very small, $[[B^2]] \sim 10^{-15}$. We define three components of the "vacuum" error,

$$E_\alpha \equiv V^{-1} \int_{\mathcal{V}} |(\nabla \times \mathbf{B}) \cdot \nabla\alpha| \, dv, \tag{22}$$

for $\alpha \in \{s, \theta, \phi\}$, and show in Fig. 2 that these decrease as the numerical Fourier resolution is increased in both the plasma, $v = 1$, and the vacuum, $v = 2$, region. The Chebyshev resolution was kept high enough, $L = 8$, to ensure a constant decrease of the error with Fourier resolution.

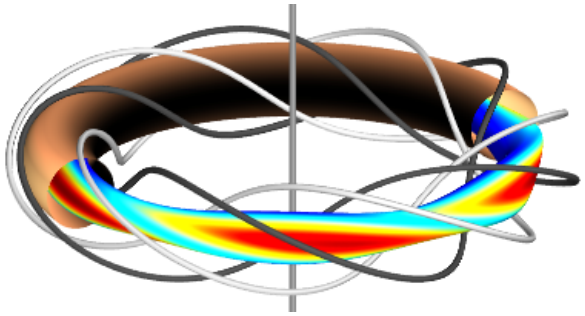

FIG. 1: Coil configuration used to produce input to SPEC for the self-verification case. A vertical wire produces the main toroidal magnetic field. The remaining field is produced by two helical windings with opposite currents. Shown are also the computational boundary used in SPEC (outer surface) and the magnitude of the magnetic field on an inner surface.

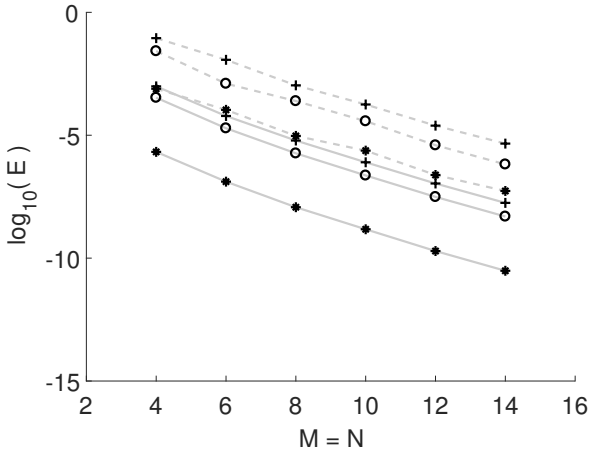

FIG. 2: E_s (crosses), E_θ (circles) and E_ϕ (stars) as defined in Eqn. 22 as a function of Fourier resolution $M = N$, in the plasma, $v = 1$ (solid lines), and vacuum, $v = 2$ (dashed lines), regions.

B. Verification with analytical solution

Dommaschk potentials [63] can be used to construct a suitable analytical solution for a stellarator-like vacuum field. We choose a set of Dommaschk potentials that generate an $\ell = 2$ classical stellarator vacuum field (this construction is described in the Appendix) with regions of magnetic surfaces, magnetic islands, and magnetic field-line chaos.

The computational boundary, $\mathcal{D}$, in SPEC is chosen to be circular, with $R = 1 + 0.2\cos(\theta)$ and $Z = -0.2\sin(\theta)$, see Fig. 3. The Fourier harmonics, $D_{C,i}$, of the differential flux produced at $\mathcal{D}$ and the total linking current, G, are obtained from the analytical solution. We again compute an equilibrium with a single plasma region, $N_V = 1$, and choose $\Psi = 0.01\Psi_0$, where Ψ_0 is the toroidal flux passing through the surface defined by $\mathcal{D}$ at the toroidal angle $\phi = 0$. Fig. 4 shows Poincaré plots obtained from the magnetic field produced by SPEC, $\mathbf{B}_S$, and by the Dommaschk potentials, $\mathbf{B}_D$, which are indistinguishable on the scale of the figure. The rotational transform profiles for both fields are shown in Fig. 5.

A quantitative measure of the difference between the two solutions is, for example, the relative difference in the magnitude of $\mathbf{B}$ at each point in space,

$$E \equiv |B_S - B_D|/B_D \tag{23}$$

where B_S is the amplitude of the field from SPEC and B_D is the amplitude of the field from the Dommaschk solution. Fig. 6 shows that both the maximum value and volume-average of E decrease as the Fourier resolution is increased (for fixed Chebyshev resolution of $L = 8$).

Further increasing the Fourier and Chebyshev resolutions results in ill-posed matrices in the innermost toroidal region, which contains the coordinate singularity. This is a known issue [64] for the class of radial basis function that were used to enforce regularity at the origin: the $\bar{s}^{m/2}$ factor included to ensure analyticity of the vector potential at the origin approaches zero almost everywhere for $\bar{s} \leq 1$ as m increases. Better radial basis functions are available, namely Zernike polynomials, and these will be implemented in future work.

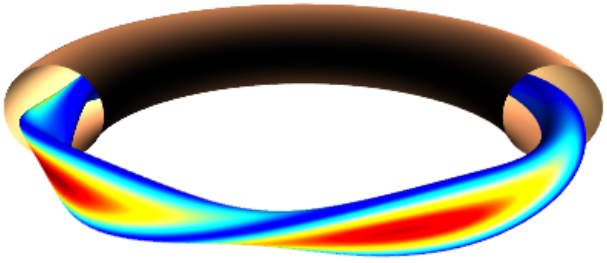

FIG. 3: Computational boundary (outer surface) used for the comparison of SPEC against the Dommaschk analytical solution. The amplitude of the magnetic field from the analytical solution is shown on an inner surface.

C. Comparison to Biot-Savart

Vacuum magnetic fields can also be calculated using the Biot-Savart law,

$$\mathbf{B}(\bar{\mathbf{x}}) = \frac{1}{4\pi}\int \frac{\mathbf{j}(\mathbf{x}) \times \mathbf{r}}{r^3} dv, \tag{24}$$

given the current density, $\mathbf{j}(\mathbf{x})$, where $\mathbf{r} \equiv \bar{\mathbf{x}} - \mathbf{x}$. The FOCUS code [65] is used to construct a suitable set of

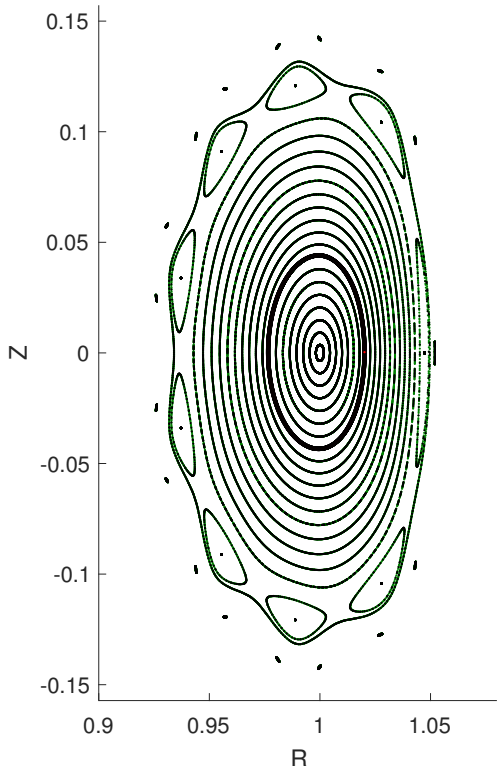

FIG. 4: Poincaré plot of the magnetic field lines for the SPEC solution (black) and the analytical solution (green). The plasma boundary is also shown (thick black line).

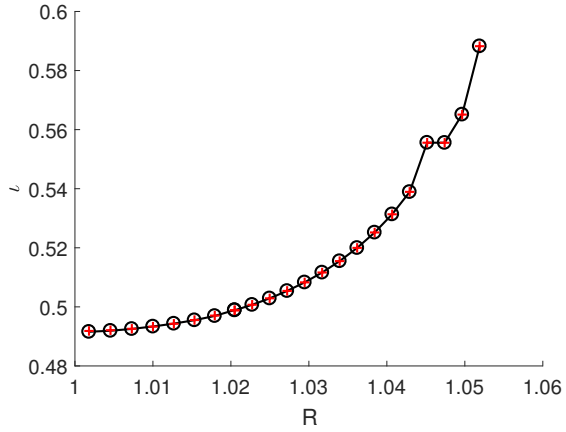

FIG. 5: Rotational transform profile for the SPEC solution (black circles) and the analytical solution (red crosses).

external currents that produce a vacuum field with a significant volume of flux surfaces and with significant rotational transform. (By "suitable", we mean suitable for the verification calculation, and for this we want to reduce the ripple associated with the finite number of coils; so, we construct a coil set with 256 coils. This coil set is unlikely to be suitable from an engineering perspective.) The configuration is shown in Fig. 7. A non-stellarator-symmetric "target surface" is provided as input to FOCUS. This will test the non-stellarator-symmetric capability in SPEC. Neither the target surface provided to FOCUS nor the coil geometry are required for the SPEC calculation.

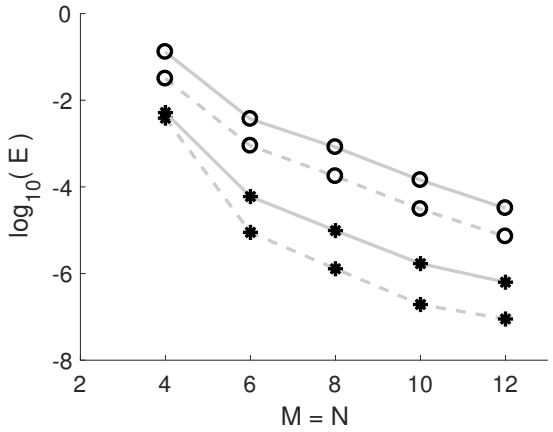

FIG. 6: Average (dashed) and maximum (solid) errors as defined by Eqn. 23 between the SPEC solution and the analytical solution in the $v = 1$ (stars) and $v = 2$ (circles) SPEC volumes, as a function of the Fourier resolution in SPEC.

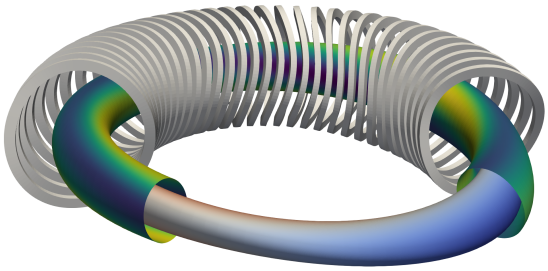

FIG. 7: Configuration for the Biot-Savart verification calculation. To produce the external field, 256 modular coils were used to reduce ripple; for clarity only 32 are shown. The outer surface is the computational boundary, the color indicates D_C, and the inner surface is the plasma boundary, and the color indicates $|\mathbf{B}|$.

The chosen computational boundary is slightly larger than the target surface provided to FOCUS, and it is not a flux surface of the vacuum field computed using Biot-Savart, and so $D_C \neq 0$.

For this calculation, we partition the plasma into two regions, i.e., $N_V = 2$. This is sufficient to test the numerical calculation in the innermost, simple-torus region, $\mathcal{V}_1$, the toroidal annular region(s), $\mathcal{V}_v$ for $v = 2, \ldots, N_V$, and the vacuum region, $\mathcal{V}_v$ for $v = N_V + 1$. The calculation in $\mathcal{V}_1$ is distinct because of the inclusion of the regularization factors, and the calculation in the vacuum region is distinct because of the non-zero differential flux allowed at the outer boundary. Adding additional regions merely adds additional annular regions and does not exercise additional capability of the algorithm.

For this $N_V > 1$ calculation, to ensure that there are no

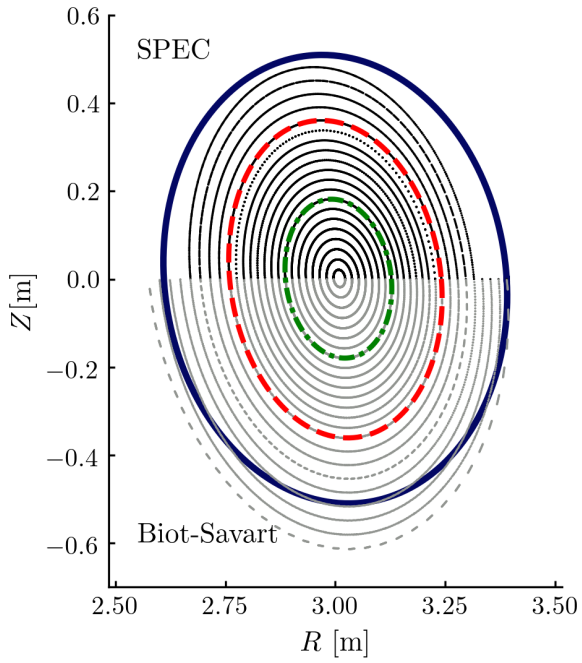

FIG. 8: Poincaré plots of the SPEC (upper) and the Biot-Savart (lower) magnetic fields using the coils shown in Fig. 7, integrated from the same starting positions. The outermost dark blue ellipse is the computational boundary, the dashed red ellipse is the plasma boundary, and the green dash-dotted ellipse is the internal interface.

currents in the calculation, it is *not sufficient* to set $I = 0$, $p_v = 0$, $\mu_v = 0$, $I = 0$, and $D_P = 0$. Doing so does ensure that there is no net toroidal plasma current, no force-free currents in the plasma volumes, no pressure-driven sheet currents, and no contribution to the differential flux at $\mathcal{D}$ produced by plasma currents; but, this does not ensure that there are no *force-free* sheet currents on each interface. Force-free sheet currents can produce discontinuities in the rotational transform. The existence of any plasma currents means that the computed magnetic field is not a vacuum magnetic field.

The net toroidal sheet current, I_v, on an interface, $\mathcal{I}_v$, is computed by considering an infinitesimally thin cross-sectional surface on, for example, the $\phi = 0$ plane with inner boundary just inside $\mathcal{I}_v$ and outer boundary just outside and is given by

$$I_v \equiv \int_0^{2\pi} \left(\mathbf{B}^+ - \mathbf{B}^-\right) \cdot \mathbf{e}_\theta \, d\theta, \tag{25}$$

where $\mathbf{B}^+$ is the tangential field immediately outside $\mathcal{I}_v$ in region $\mathcal{V}_{v+1}$ and $\mathbf{B}^-$ is the tangential field immediately inside $\mathcal{I}_v$ in region $\mathcal{V}_v$. To recover the vacuum solution, these must all be zero.

Because there is only one poloidal flux profile (and one rotational-transform profile) that is consistent with a given toroidal flux profile for a given vacuum field, generally an iterative search for the appropriate value of $\Delta\psi_{p,v}$ for the given $\Delta\psi_{t,v}$ is required to ensure that $I_v = 0$. To clarify: in this $N_V = 2$ calculation, $\Delta\psi_{p,2}$ is adjusted to ensure that $I_1 = 0$, and the values of $\Delta\psi_{t,3}$ and $\Delta\psi_{p,3}$, namely the toroidal and poloidal "fluxes" in the vacuum region, are adjusted to ensure $I = 0$ and to obtain the prescribed linking current, G. Then, it is guaranteed that $I_2 = 0$.

A comparison of the Poincaré plots associated with the vacuum magnetic field calculated by SPEC, $\mathbf{B}_S$, and that calculated using the Biot-Savart law given the coil geometries and currents, $\mathbf{B}_C$, is shown in Fig. 8. On this scale, the Poincaré plots are identical. Fig. 9 shows the quantitative error,

$$E \equiv V^{-1} \int_{\mathcal{V}} |\mathbf{B}_S - \mathbf{B}_C| \, dv, \tag{26}$$

plotted against Fourier resolution.

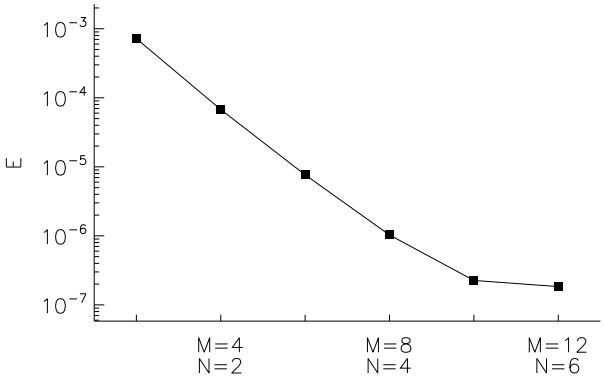

FIG. 9: Error between the SPEC magnetic field and the Biot-Savart field as defined in Eqn. 26 plotted against Fourier resolution.

This error reliably decreases as the numerical resolution is increased, at least up to the point where the error becomes dominated by the Chebyshev resolution. The radial (Chebyshev) resolution is $L = 8$ in each region.

D. Verification of the virtual casing calculation

For the above vacuum calculations, it was not required to calculate the differential flux at $\mathcal{D}$ produced by the plasma currents. The vacuum solution was sought, so it was appropriate and expedient to assume $D_P = 0$. Generally, $D_P \neq 0$, and D_P must be computed at each free-boundary iteration using the virtual-casing principle. To separately verify that the virtual-casing algorithm in SPEC is correctly implemented, we describe an example calculation.

We consider a circular wire at fixed $R = R_0 = 6$ and $Z = 0$ carrying a current I_W. The differential flux, D_P, produced by this wire on a given computational boundary, $\mathcal{D}$, can be calculated analytically, and we choose an elliptical computational boundary given by $R = 6 + 3\cos(\theta)$ and $Z = -4\sin(\theta)$. The arrangement is illustrated in Fig. 10.

SPEC can be used to approximate the magnetic field produced by this circular wire. We choose $N_V = 1$, the pressure to be $p = 0$, and the plasma boundary to be a circular cross-section, axisymmetric torus, namely

$R = R_0 + a\cos(\theta)$ and $Z = -a\sin(\theta)$, were the value of the minor radius, a, can in principle be made arbitrarily small in order to approach the "wire limit". Since only the virtual casing calculation is to be tested, the geometry of the plasma boundary is not adjusted to satisfy force balance.

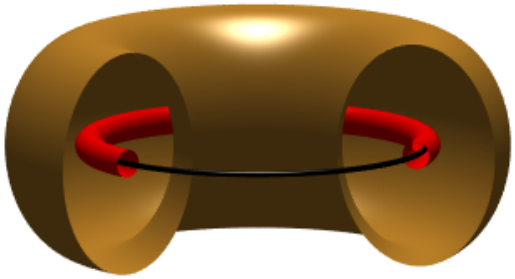

FIG. 10: Configuration considered for the "wire model". Shown are the computational boundary (outer surface), an example of plasma boundary for $a = 0.5$ (red inner surface), and the circular current-carrying wire (black).

The total toroidal flux is chosen as $\Psi = (a/a_0)^2\Psi_0$, with Ψ_0 the toroidal flux passing through the surface defined by $\mathcal{D}$ at the toroidal angle $\phi = 0$, and $a_0 = 3$. The exact value is not important but the scaling with a^2 ensures that toroidal magnetic field does not diverge as we take the limit $a \to 0$. The toroidal plasma current is set equal to that of the wire by choosing $I = I_W$ and $\mu\Psi = I_W$. In the limit $a \to 0$, SPEC should produce the same magnetic field as the circular wire. We define the relative errors in the different poloidal harmonics of D_P between the analytical wire model, $D^W_{P,m}$, and the SPEC calculation, $D^S_{P,m}$, namely

$$E_m \equiv |D^S_{P,m} - D^W_{P,m}|/D^W_{P,m} \ . \tag{27}$$

Fig. 11 shows how these errors decrease with decreasing plasma size, as expected. The numerical resolution parameters used in SPEC are $M = 10$, $N = 0$ and $L = 8$, and the results in Fig. 11 do not change with increasing resolution.

Additional verification calculations, which will not be described here for sake of brevity, of the virtual casing calculation were performed against the DIAGNO code [66].

E. Verification of a free-boundary equilibrium against analytical theory

A verification of a tokamak-like free-boundary equilibrium against analytical theory is possible by extending the circular-wire model described above. This "plasma wire" cannot be in equilibrium unless a suitable vertical field, B_V, is externally applied. For $B_V = 0$ the plasma column would expand in the R direction (due to the so-called hoop force). For a large-aspect-ratio tokamak plasma with circular cross-section, the required B_V

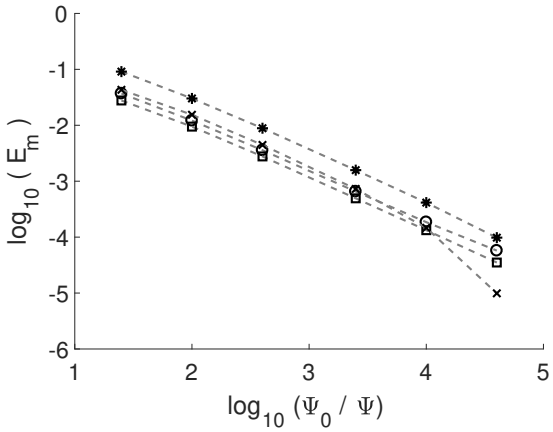

FIG. 11: Relative errors E_m as defined in Eqn. 27 for $m = 1$ (circles), $m = 2$ (squares), $m = 3$ (stars), and $m = 4$ (crosses). The ratio Ψ_0/Ψ scales as $1/a^2$.

to maintain a plasma of size a carrying a toroidal current I in equilibrium and centered at $R = R_0$ is given [67] by

$$B_V = \frac{\mu_0 I}{4\pi R_0}\left(\beta_p + \frac{l_i - 3}{2} + \ln\frac{8R_0}{a}\right), \tag{28}$$

where $l_i \equiv 2\int_0^a B_\theta^2 \ r\,dr/a^2B_\theta^2(a)$ is the normalized internal plasma inductance per unit length and here $\beta_p = 0$ since we are considering zero plasma pressure. By taking the large-aspect-ratio limit of the Beltrami equation, the poloidal field is given analytically by $B_\theta(r) = B_\theta(a)J_1(\mu r)/J_1(\mu a)$, with J_n the Bessel function of the first kind, and the inductance is $l_i = 1 - J_0(\mu a)\,J_2(\mu a)/J_1^2(\mu a)$. Given the plasma current, I, and the enclosed toroidal flux, Ψ, which determines μ via $\mu\Psi = I$, we can therefore write the required vertical field as a function of R_0 and a, i.e., $B_V = B_V(R_0, a)$. SPEC is run to compute free-boundary equilibria with different values of externally imposed B_V to verify that the different equilibrium plasma positions and sizes, namely R_0 and a, satisfy Eqn. 28. In order to prescribe B_V in the SPEC calculations we analytically evaluate the Fourier harmonics $D_{C,i}$ of the differential flux produced by this field on $\mathcal{D}$.

Fig. 12 shows the comparison between the value of B_V used in SPEC and the value predicted by Eqn. 28. The agreement is as expected. The analytical theory is based on an expansion in the inverse aspect ratio, $\epsilon = a/R_0$, and thus an error of the order of ϵ^2 is expected. B_V is scanned over a large range of values and the plasma column significantly moves and changes size as B_V is varied.

F. VMEC-SPEC verification

Our final verification calculation is between the free-boundary SPEC code and the free-boundary VMEC code. An appropriate free-boundary VMEC equilibrium

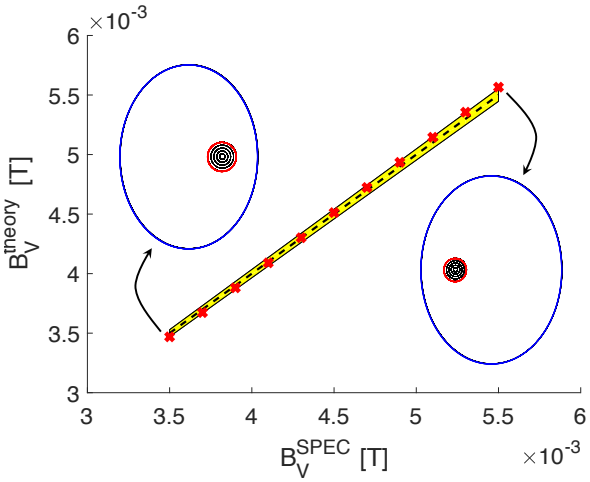

FIG. 12: Comparison between predicted (y-axis) and obtained (x-axis) vertical field required to center a circular plasma of size a with major radius R. The dashed line indicates perfect agreement, namely $y = x$, and the yellow band shows the amplitude of a relative error of order ϵ^2. The position and size of the plasma is shown for the two extreme values of the vertical field, with the elliptical computational boundary in blue.

[43] and coil set is constructed by first choosing an axisymmetric fixed-boundary VMEC equilibrium, in this case the Solovev equilibrium [68], then computing the normal field on the plasma boundary produced by plasma currents using the BNORM [69] code, and then using FOCUS to compute a set of external current-carrying coils that provides the appropriate vacuum field (so that the total normal field on the plasma boundary is zero, as best as possible). Instead of a using a finite set of modular coils, which would result in a non-zero amount of non-axisymmetric ripple, an infinite vertical current filament was placed in the center, as shown in Fig. 13.

A high-resolution free-boundary VMEC calculation is performed (including the poloidal Fourier harmonics $m \in \{0, 1, \ldots, 31\}$ and with 2048 radial surfaces) using a high-resolution "mgrid" file ($N_R = 801, N_Z = 801$). The pressure profile supplied to VMEC is $p(\psi) = 1 - \psi$, and the rotational transform profile is $\iota(\psi) = 0.49 - 0.3\psi$, where ψ is the normalized toroidal flux, and the total enclosed toroidal flux is 1.0Wb.

The pressure profile supplied to SPEC is a stepped approximation to the VMEC pressure profile. Note that because the pressure profile in SPEC is necessarily discontinuous, whereas the pressure profile used in the VMEC calculation is continuous and differentiable, there is necessarily a difference in the computed equilibria. This difference should reduce as the number of interfaces is increased, provided that the Fourier resolution is sufficiently large.

The SPEC inputs are constructed by first choosing the number of plasma volumes, $N_V = 2, 4, \ldots, 128$. The enclosed toroidal flux in each region, $\Delta\psi_{t,v}$ for $v = 1, \ldots, N_V$, is chosen so that the 'effective minor radius' is equally spaced, i.e., $\psi_{t,v} = \Psi\sqrt{v/N_V}$, where $\psi_{t,v} = \psi_{t,v-1} + \Delta\psi_{t,v}$ and $\psi_{t,0} = 0$. The SPEC calculation includes the poloidal modes $m \in \{0, 1, \ldots, 32\}$. The required Chebyshev resolution depends on N_V. For the calculation with $N_V = 2$, we choose $L_1 = 4$, $L_2 = 12$ and $L_3 = 20$. As N_V increases, the Chebyshev resolution in each volume can be allowed to decrease, and for the $N_V = 128$ calculation we choose $L_v = 2, 4, 4, \ldots, 20$. The stepped-pressure profile, namely the p_v, supplied to SPEC is chosen so that

$$p_v \, \Delta\psi_{t,v} = \int_{\psi_{t,v-1}}^{\psi_{t,v}} p(\psi) d\psi, \tag{29}$$

and the (continuous) rotational transform on each interface is $\iota_v \equiv \iota(\psi_{t,v})$.

For $\mathcal{D}$ we choose a circular cross-section axisymmetric toroidal surface of major radius $R_0 = 3.999m$ and minor radius $r = 1.8m$. The initial geometry of the SPEC interfaces is that of nested, circular cross section, axisymmetric tori.

The initial guess for the normal field on $\mathcal{D}$ produced by the plasma currents is constructed as follows. First we compute a fixed-boundary SPEC equilibrium consistent with the boundary extracted from the free-boundary VMEC equilibrium. Then, we use the virtual casing method implemented in SPEC using the tangential magnetic field on the inner side of the plasma boundary. This is a good approximation and is sufficient to initialize the free-boundary SPEC calculation; but, as described earlier, to ensure that the virtual casing integral incorporates sheet currents that might lie of the plasma boundary, the correct tangential field to use in the virtual casing integral is that immediately outside the plasma boundary. The Picard-blend parameter is $\lambda = 0.4$. As we increase the number of volumes, the free-boundary SPEC calculation is initialized with the lower resolution converged equilibrium; for example, the $N_V = 16$ calculation is initialized using the $N_V = 8$ solution, and the Picard-blend parameter can decrease (as the initial guess improves). An example Poincaré plot showing the flux surfaces are shown in Fig. 14.

The error between the VMEC and SPEC equilibria is computed as

$$E \equiv \sum_{v=1}^{N_V} \oint |\mathbf{x}_{S,v}(\theta, 0) - \mathbf{x}_V(\psi_{t,v}, \bar{\theta}, 0)| dl, \tag{30}$$

where $\mathbf{x}_{S,v}(\theta, \phi)$ is the geometry of the v-th interface, i.e., $\mathcal{I}_v$, and $\mathbf{x}_V(\psi_{t,v}, \bar{\theta}, \phi)$ is the geometry of the corresponding VMEC surface, and dl is the infinitesimal arc-length. (Note that in computing this quantity it is required to accommodate the fact that VMEC and SPEC use different poloidal parameterizations.) This error, and a similar error computed on only the midpoint interface, i.e., with the lower and upper summation limits in Eqn. 30 replaced by $v = N_V/2$ to $v = N_V$, are shown in Fig. 15. The latter construction avoids the region near the magnetic axis, which seems to be limiting the decrease of the error as N_V increases.

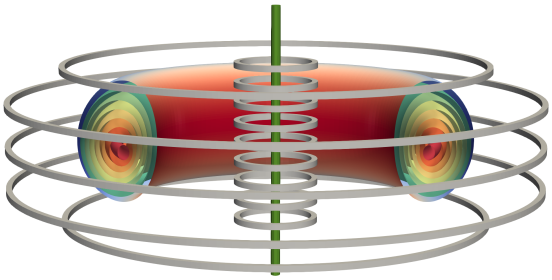

FIG. 13: The current-carrying coils used for the free-boundary VMEC-SPEC verification calculation. To avoid toroidal ripple, the toroidal field is provided by a vertical filament. The SPEC interfaces are also shown. The colors on the outermost surface indicate $|\mathbf{B}_C|$.

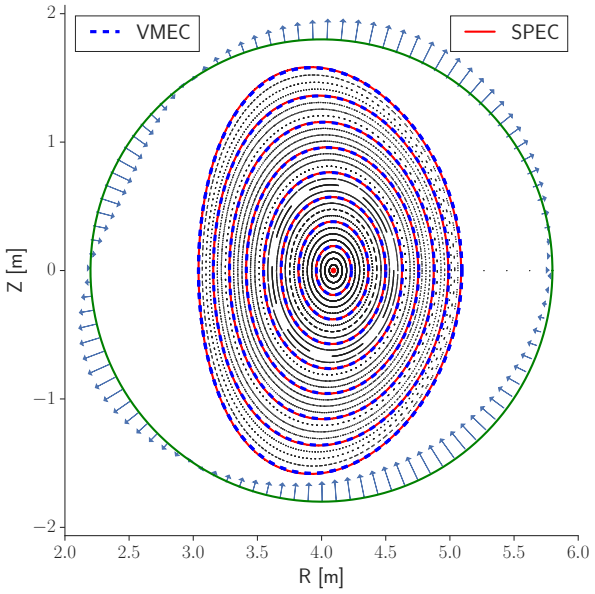

FIG. 14: Poincaré plot for free-boundary VMEC-SPEC verification showing the $N_V = 8$ SPEC calculation. The computational boundary, $\mathcal{D}$, is shown as the outer, circular surface. The SPEC interfaces are shown as solid lines, the corresponding VMEC surfaces as thick dashed lines, and a Poincaré plot of the SPEC magnetic field is shown with gray dots. (In the vacuum region, the fieldlines leave the domain and these fieldlines are not shown.) The arrows on the computational boundary indicate the differential flux from the coils, $\mathcal{D}_C$.

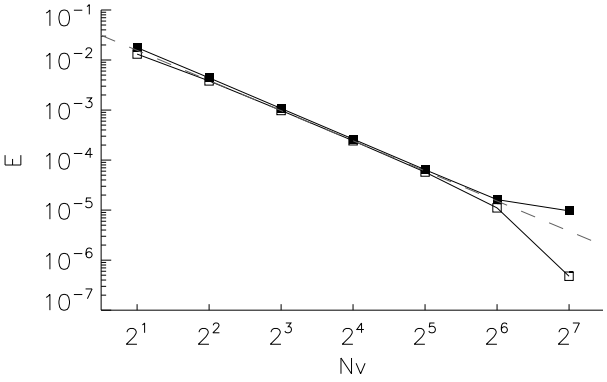

FIG. 15: Error as defined in Eqn. 30 between the SPEC magnetic field and the VMEC field. The dashed line has slope $= -2$. When the region near the magnetic axis is excluded from the calculation, the error seems to decrease more favorably (open squares).

V. COMMENTS

An immediate physics application for free-boundary SPEC is to explicitly calculate the effect of resonant magnetic perturbations [70] on the unstable manifold [71] surrounding the plasma. We will use SPEC to understand sawteeth-like relaxation events in W7-X, and in equilibrium reconstruction and stellarator optimization calcuations.

In the development of SPEC thus far, we have given priority to functionality and accuracy. Now that the free-boundary, non-stellarator-symmetric capability in SPEC has been verified, our code development efforts will shift to, for example, making the numerical calculation more efficient (by exploiting symmetries in the metric coefficients, for example) and more robust (by implementing additional numerical algorithms for finding minima of the energy functional).

There are also various weaknesses in SPEC that will be addressed. In a future paper we will describe the use of Zernike polynomials in the innermost volume [64]. The presently implemented coordinate interpolation in the innermost volume can cause problems: if the plasma boundary is strongly shaped and only one plasma volume is used, the geometric center of the innermost interface is not guaranteed to be a suitable coordinate axis. In future, we intend to revise the toroidal angle parameterization (and the spectral condensation constraints) for numerical efficiency and so that arbitrary knotted equilibria [72] can be computed.

It will be interesting to study particle orbits across the MRxMHD interfaces, and their motion in stochastic fields and across magnetic islands. In future work we will report the coupling of SPEC equilibrium to the VENUS code [73] so that this topic may be explored. Given that MRxMHD has astrophysical relevance, a longer term development goal of SPEC is to change the periodic boundary conditions to line-tied boundary conditions, and to investigate MRxMHD phenomena in solar-flares, for example.

This manuscript is based upon work supported by the U.S. Department of Energy, Office of Science, Office of Fusion Energy Sciences, and has been authored by Princeton University under Contract Number DE-AC02-09CH11466 with the U.S. Department of Energy. This work has also been carried out within the framework of the EUROfusion Consortium and has received funding from the Euratom research and training programme 2014-2018 and 2019-2020 under grant agreement No 633053. The views and opinions expressed herein do not necessarily reflect those of the European Commission. This work is partly funded by Australian ARC project

DP170102606. This work was also supported by a grant from the Simons Foundation/SFARI (560651, AB).

[1] J. R. Cary and R. G. Littlejohn. Noncanonical Hamiltonian mechanics and its application to magnetic field line flow. *Ann. Phys.*, 151:1, 1983.

[2] A. J. Lichtenberg and M. A. Lieberman. *Regular and Chaotic Dynamics, 2nd ed.* Springer-Verlag, New York, 1992.

[3] J. D. Meiss. Symplectic maps, variational principles & transport. *Rev. Mod. Phys.*, 64(3):795, 1992.

[4] J. Moser. *Stable and Random Motions.* Princeton Univ. Press,, Princeton, N. J., 1973.

[5] V. I. Arnold. *Mathematical methods of Classical Mechanics.* Springer-Verlag Press, New York, 1978.

[6] S. Aubry. The twist map, the extended Frenkel-Kontorova model and the Devils Staircase. *Physica D*, 7(1-3):240, 1983.

[7] J. N. Mather. Existence of quasi-periodic orbits for twist homeomorphisms of the annulus. *Topology*, 21:457, 1982.

[8] I. C. Percival. Variational principles for invariant tori and cantori. In M. Month and J. C. Herra, editors, *Nonlinear Dynamics and the Beam-Beam interaction*, volume 57 of *AIP Conf. Proc.*, New York, 1979. AIP.

[9] S. R. Hudson. Calculation of cantori for Hamiltonian flows. *Phys. Rev. E.*, 74:056203, 2006.

[10] J. D Meiss. Class renormalization: islands around islands. *Phys. Rev. A.*, 34(3):2375, 1986.

[11] W. A. Newcomb. Magnetic diferential equations. *Phys. Fluids*, 2(4):362, 1959.

[12] S. R. Hudson. A regularized approach for solving magnetic differential equations and a revised iterative equilibrium algorithm. *Phys. Plasmas*, 17:114501, 2010.

[13] H. Grad. Toroidal containment of a plasma. *Phys. Fluids*, 10(1):137, 1967.

[14] A. Bhattacharjee, T. Hayashi, C. C. Hegna, N. Nakajima, and T. Sato. Theory of pressure-induced islands and self-healing in three-dimensional toroidal magnetohydrodynamic equilibria. *Phys. Plasmas*, 2(3):883, 1995.

[15] S. R. Hudson, R. L. Dewar, G Dennis, M. J. Hole, M. McGann, G. von Nessi, and S. Lazerson. Computation of multi-region relaxed magnetohydrodynamic equilibria. *Phys. Plasmas*, 19:112502, 2012.

[16] Potter. Waterbag methods in magnetohydrodynamics. *Methods Comp. Phys.*, 16:43, 1976.

[17] H. L. Berk, J. P. Freidberg, X. Llobet, P. J. Morrison, and J. A. Tataronis. Existence and calculation of sharp boundary magnetohydrodynamic equilibrium in three-dimensional toroidal geometry. *Phys. Fluids*, 29(10):3281, 1986.

[18] O. P. Bruno and P. Laurence. Existence of three-dimensional toroidal MHD equilibria with nonconstant pressure. *Commun. Pur. Appl. Math.*, 49(7):717, 1996.

[19] M. J. Hole, S. R. Hudson, and R. L. Dewar. Stepped pressure profile equilibria in cylindrical plasmas via partial Taylor relaxation. *J. Plasma Phys.*, 72(6):1167, 2006.

[20] M. J. Hole, S. R. Hudson, and R. L. Dewar. Equilibria and stability in partially relaxed plasma-vacuum systems. *Nucl. Fus.*, 47:746, 2007.

[21] S. R. Hudson, M. J. Hole, and R. L. Dewar. Eigenvalue problems for Beltrami fields arising in a three-dimensional toroidal magnetohydrodynamic equilibrium problem. *Phys. Plasmas*, 14:052505, 2007.

[22] M. D. Kruskal and R. M. Kulsrud. Equilibrium of a magnetically confined plasma in a toroid. *Phys. Fluids*, 1(4):265, 1958.

[23] J. B Taylor. Relaxation of toroidal plasma and generation of reverse magnetic-fields. *Phys. Rev. Lett.*, 33:1139, 1974.

[24] J. B Taylor. Relaxation and magnetic reconnection in plasmas. *Rev. Mod. Phys.*, 58:741, 1986.

[25] R.L. Mills, M.J. Hole, and R.L. Dewar. Magnetohydrodynamic stability of plasmas with ideal and relaxed regions. *J. Plasma Phys.*, 2009.

[26] D. Barmaz. High-n stability of a pressure discontinuity in a three-dimensional plasma. Master's thesis, "Ecole Polytechnique Fédérale de Lausanne (EPFL), Centre de Recherche en Physique des Plasmas, CH1015, Lausanne, Switzerland, 2011.

[27] G. R. Dennis, S. R. Hudson, R. L. Dewar, and M. J. Hole. Multi-region relaxed magnetohydrodynamics with flow. *Phys. Plasmas*, 21(4):042501, 2014.

[28] G. R. Dennis, S. R. Hudson, R. L. Dewar, and M. J. Hole. Multi-region relaxed magnetohydrodynamics with anisotropy and flow. *Phys. Plasmas*, 21(7):072512, 2014.

[29] M. Lingam, H. M. Abdelhamid, and S. R. Hudson. Multi-region relaxed Hall magnetohydrodynamics with flow. *Phys. Plasmas*, 23(8):082103, 2016.

[30] R.L. Dewar, Z. Yoshida, A. Bhattacharjee, and S.R. Hudson. Variational formulation of relaxed and multi-region relaxed magnetohydrodynamics. *J. Plasma Phys.*, 81:515810604, 2015.

[31] S. R. Hudson and B. Kraus. Three-dimensional magnetohydrodynamic equilibria with continuous magnetic fields. *J. Plasma Phys.*, 83:715830403, 2017.

[32] A. M. Wright, S. R. Hudson, R. L. Dewar, and M. J. Hole. Resistive stability of cylindrical MHD equilibria with radially localized pressure gradients. *Phys. Plasmas*, 26(6):062117, 2019.

[33] G. R. Dennis, S. R. Hudson, D. Terranova, P. Franz, R. L. Dewar, and M. J. Hole. Minimally constrained model of self-organized helical states in reversed-field pinches. *Phys. Rev. Lett.*, 111:055003, 2013.

[34] J. Loizu, S. R. Hudson, A. Bhattacharjee, and P. Helander. Magnetic islands and singular currents at rational surfaces in three-dimensional MHD equilibria. *Phys. Plasmas*, 22:022501, 2015.

[35] G. R. Dennis, S. R. Hudson, R. L. Dewar, and M. J. Hole. The infinite interface limit of multiple-region relaxed magnetohydrodynamics. *Phys. Plasmas*, 20:032509, 2013.

[36] J. Loizu, S. R. Hudson, A. Bhattacharjee, S. Lazerson, and P. Helander. Existence of three-dimensional ideal-MHD equilibria with current sheets. *Phys. Plasmas*, 22:090704, 2015.

[37] J. Loizu, S. R. Hudson, P. Helander, S. A. Lazerson, and A. Bhattacharjee. Pressure-driven amplification and penetration of resonant magnetic perturbations. *Phys. Plasmas*, 23(5):055703, 2016.

[38] J. Loizu, S. R. Hudson, and C. Nührenberg. Verification of the SPEC code in stellarator geometries. *Phys. Plasmas*, 23(11):112505, 2016.

[39] J. Loizu, S. R. Hudson, C. Nührenberg, and J. Geiger. Equilibrium β-limits in classical stellarators. *J. Plasma Phys.*, 83:715830601, 2017.

[40] J. Loizu and S. R. Hudson. Multi-region relaxed magnetohydrodynamic stability of a current sheet. *Phys. Plas-*

mas, 26:030702, 2019.
[41] J. Loizu, S. R. Hudson, Y.-M. Huang, A. Kumar, and Z. Qu. Direct prediction of nonlinear tearing mode saturation using a variational principle. *Phys. Rev. Lett.*, submitted 2020.
[42] Z. Qu, R. L. Dewar, F. Ebrahimi, J. K. Anderson, S. R. Hudson, and M. J. Hole. Stepped pressure equilibrium with relaxed flow and applications in reversed-field pinch plasmas. arXiv:2001.06984, 2020.
[43] S. P. Hirshman, W. I. van Rij, and P. Merkel. Three-dimensional free boundary calculations using a spectral Green's function method. *Comp. Phys. Comm.*, 43:143, 1986.
[44] M. Drevlak, D. Monticello, and A. Reiman. PIES free boundary stellarator equilibria with improved initial conditions. *Nucl. Fus.*, 45:731, 2005.
[45] M. G. Schlutt, C. C. Hegna, C. R. Sovinec, E. D. Held, and S. E. Kruger. Self-consistent simulations of nonlinear magnetohydrodynamics and profile evolution in stellarator configurations. *Phys. Plasmas*, 20(5):056104, 2013.
[46] Y. Suzuki, N. Nakajima, K. Watanabe, Y. Nakamura, and T. Hayashi. Development and application of HINT2 to helical system plasmas. *Nucl. Fus.*, 46:L19, 2006.
[47] H. Peraza-Rodriguez, J.M. Reynolds-Barredo, R. Sanchez, J. Geiger, V. Tribaldos, S.P. Hirshman, and M. Cianciosa. Extension of the SIESTA MHD equilibrium code to free-plasma-boundary problems. *Phys. Plasmas*, 24(8):082516, 2017.
[48] D. Malhotra, A. Cerfon, L-M. Imbert-Gérard, and Michael O'Neil. Taylor states in stellarators: A fast high-order boundary integral solver. *J. Comp. Phys.*, 397:108791, 2019.
[49] S. C. Jardin, N. Ferraro, J. Breslau, and J. Chen. Multiple timescale calculations of sawteeth and other global macroscopic dynamics of tokamak plasmas. *Comput. Sci. Disc.*, 5:014002, 2012.
[50] F. Hindenlang. *private communication.*
[51] J. M. Finn and T. M. Antonsen Jr. Magnetic helicity: What is it and what is it good for? *Comments Plasma Phys. Control. Fusion*, 9:111, 1985.
[52] David Pfefferlé and Lyle Noakes. Gauge freedom in magnetostatics and the effect on helicity in toroidal volumes. *preprint*, 2020.
[53] M. McGann, S. R. Hudson, R. L. Dewar, and G. von Nessi. Hamilton-jacobi theory for continuation of magnetic field across a toroidal surface supporting a plasma pressure discontinuity. *Phys. Lett. A*, 374(33):3308, 2010.
[54] Caoxiang Zhu, Michael Zarnstorff, David Gates, and Arthur Brooks. Designing stellarators using perpendicular permanent magnets. *arXiv:1912.05144*, 2019.
[55] R. L. Dewar and S. R. Hudson. Stellarator symmetry. *Physica D*, 112(1-2):275, 1998.
[56] S. P. Hirshman and H. K. Meier. Optimized Fourier representations for three-dimensional magnetic surfaces. *Phys. Fluids*, 28(5):1387, 1985.
[57] S. P. Hirshman and J. Breslau. Explicit spectrally optimized Fourier series for nested magnetic surfaces. *Phys. Plasmas*, 5(7):2664, 1998.
[58] V. D. Shafranov and L. E. Zakharov. Use of the virtual-casing principle in calculating the containing magnetic field in toroidal plasma systems. *Nucl. Fus.*, 12:599, 1972.
[59] S.A. Lazerson. The virtual-casing principle for 3D toroidal systems. *Plasma Phys. Contr. F*, 54:122002, 2012.
[60] J. D. Hanson. The virtual-casing principle and Helmholtz's theorem. *Plasma Phys. Contr. F*, 57:115006, 2015.
[61] C. Mercier. Equilibrium and stability of a toroidal magnetohydrodynamic system in the neighbourhood of a magnetic axis. *Nucl. Fus.*, 4(3):213, 1964.
[62] P. Helander. Theory of plasma confinement in non-axisymmetric magnetic fields. *Rep. Prog. Phys.*, 77(8):087001, 2014.
[63] Dommaschk. Representations for vacuum potentials in stellarators. *Comp. Phys. Comm.*, 40:203–218, 1986.
[64] John P. Boyd and Fu Yu. Comparing seven spectral methods for interpolation and for solving the Poisson equation in a disk: Zernike polynomials, Logan-Shepp ridge polynomials, Chebyshev-Fourier Series, cylindrical Robert functions, Bessel-Fourier expansions, square-to-disk confor. *J. Comp. Phys.*, 230(4):1408, 2011.
[65] Caoxiang Zhu, Stuart R. Hudson, Yuntao Song, and Yuanxi Wan. New method to design stellarator coils without the winding surface. *Nucl. Fus.*, 58:016008, 2018.
[66] Samuel Aaron Lazerson, S Sakakibara, and Yasuhiro Suzuki. A magnetic diagnostic code for 3D fusion equilibria. *Plasma Phys. Contr. F*, 55(2):025014, January 2013.
[67] J. P Freidberg. *Ideal Magnetohydrodynamics.* Plenum Press, New York, 1987.
[68] S. P. Hirshman and J. P Whitson. Steepest-descent moment method for three-dimensional magnetohydrodynamic equilibria. *Phys. Fluids*, 26(12):3553, 1983.
[69] P. Merkel. An integral equation technique for the exterior and interior Neumann problem in toroidal regions. *J. Comp. Phys.*, 66(1):83, 1986.
[70] I.T. Chapman, M. Becoulet, T. Bird, J. Canik, M. Cianciosa, W.A. Cooper, T. Evans, N. Ferraro, C. Fuchs, M. Gryaznevich, Y. Gribov, C. Ham, J. Hanson, G. Huijsmans, A. Kirk, S. Lazerson, Y. Liang, I. Lupelli, R.A. Moyer, C. Nührenberg, F. Orain, D. Orlov, W. Suttrop, D. Yadykin, MAST the ASDEX Upgrade, DIII-D, NSTX Teams, and EFDA-JET Contributors. Three-dimensional distortions of the tokamak plasma boundary: boundary displacements in the presence of resonant magnetic perturbations. *Nucl. Fus.*, 54:083006, 2014.
[71] R. K.W. Roeder, B. I. Rapoport, and T. E. Evans. Explicit calculations of homoclinic tangles in tokamaks. *Phys. Plasmas*, 10(9):3796, 2003.
[72] S. R. Hudson, E. Startsev, and E. Feibush. A new class of magnetic confinement device in the shape of a knot. *Phys. Plasmas*, 21:010705, 2014.
[73] D.Pfefferlé, W.A.Cooper, J.P.Graves, and C.Misev. Venus-levis and its spline-fourier interpolation of 3d toroidal magnetic field representation for guiding-centre and full-orbit simulations of charged energetic particles. *Comp. Phys. Comm.*, 185(12):3127–3140, 2014.
[74] W. Dommaschk. IPP-Report 0/48 (table IV) 20, 1984.
[75] C. Gourdon. Configurations du type stellarator avec puits moyen et cisaillement des lignes magnetiques. *Proc. 3rd Int. Conf. Plasma Phys. Control. Nucl. Fusion Res., Novosibirsk, USSR*, 1:847, 1968.

1. Appendix: Stellarator vacuum fields from Dommaschk potentials

A vacuum magnetic field is given by its scalar potential, $\mathbf{B} = \boldsymbol{\nabla}\Phi$, with $\nabla^2\Phi = 0$. Following Dommaschk's paper [63], we write

$$\Phi \;=\; \phi + \sum_{m,l} \Phi_{m,l}(R,\phi,Z), \tag{31}$$

with (R, ϕ, Z) cylindrical coordinates and the $\Phi_{m,l}$ separate solutions of the Laplace equation, $\nabla^2 \Phi_{m,l} = 0$. In a stellarator with a single magnetic axis and N_P field periods, the value of m in Eqn. 31 is an integer multiple of N_P, and $l = 0, 1, 2, \ldots$

The classical, $\ell = 2$, 5-period stellarator used for the verification calculation is "DOM25B", and is given by $m = 5$, $A^1_{5,2} = A^2_{5,2} = -1.489$ in Ref.[74], namely,

$$\Phi_{m,l} \;=\; A^1_{m,l} D_{m,l} \sin(m\phi) + A^2_{m,l} N_{m,l-1} \cos(m\phi) \quad (32)$$

The functions $D_{m,l}$ and $N_{m,l-1}$ in Eqn. 32 can be generated recursively. Using Eqn. 32, we have

$$D_{m,2} \;=\; C^D_{m,0} \, \frac{Z^2}{2} + C^D_{m,1} \quad (33)$$

$$N_{m,1} \;=\; C^N_{m,0} \, Z \quad (34)$$

with

$$C^D_{m,0} \;=\; (R^m + R^{-m})/2, \quad (35)$$

$$C^N_{m,0} \;=\; (R^m - R^{-m})/(2m), \quad (36)$$

$$C^D_{m,1} \;=\; [c_1 R^{m+2} + c_2 R^m + c_3 R^{-m+2} + c_4 R^{-m}] \;/\; [8m(m^2-1)], \quad (37)$$

where $c_1 = -m(m-1)$, $c_2 = (m+1)(m-2)$, $c_3 = m(m+1)$, and $c_4 = -(m+2)(m-1)$. The result of tracing field lines in the vacuum field for DOM25B is shown in Fig. 4 and Fig. 5, showing respectively the Poincaré plot and the rotational transform profile. The field-line tracer used is the GOURDON code [75].